Journal of ELECTRONIC MATERIALS, Vol. 44, No. 1, 2015
DOI: 10.1007/s11664-014-3511-9

Engineering the Bandgap of Unipolar HgCdTe-Based nBn Infrared Photodetectors

M. KOPYTKO,[1,4] J. WRÓBEL,[1] K. JÓŹWIKOWSKI,[1] A. ROGALSKI,[1] J. ANTOSZEWSKI,[2] N.D. AKHAVAN,[2] G.A. UMANA-MEMBRENO,[2] L. FARAONE,[2] and C.R. BECKER[3]

1.—Institute of Applied Physics, Military University of Technology, 2 Kaliskiego St., 00-908 Warsaw, Poland. 2.—School of Electrical, Electronic and Computer Engineering, The University of Western Australia, 35 Stirling Highway, Crawley 6009, Australia. 3.—Physics Department, University of Illinois at Chicago, Chicago, IL 60607-7059, USA. 4.—e-mail: mkopytko@wat.edu.pl

Design of practically realizable unipolar HgCdTe nBn photodetectors has been studied in detail by numerical analysis. The simulations reported herein reveal that, by optimization of barrier doping, dark current levels can be reduced and collection efficiency substantially improved. It is shown that *p*-type doping of the barrier layer can significantly reduce the effective potential barrier arising from the valence band offset between the absorber and barrier regions, thus enabling HgCdTe nBn detector operation under near zero-bias conditions. However, relatively high electric fields in the space charge regions near the barrier/absorber interface result in enhanced trap-assisted Shockley–Read–Hall thermal generation. Our calculations indicate that nBn HgCdTe detectors with barriers engineered by use of HgTe/$Hg_{0.05}Cd_{0.95}Te$ superlattices have, potentially, substantially better valence band alignment without the need for *p*-type doping.

Key words: HgCdTe, nBn detectors, barrier detectors, valence band energy barrier

INTRODUCTION

The unipolar nBn photodetector structure, first reported by Maimon and Wicks,[1] can be used to substantially reduce dark current and noise without impeding photocurrent flow. The nBn photodetector can be regarded as topologically similar to a homojunction *p*-*n* photodiode, with the space charge region and *p*-type contact layer in the latter replaced by a unipolar bandgap barrier (B) and an *n*-contact layer, respectively. The unipolar barrier is engineered to block most of the carrier electron flow while being no barrier to the flow of minority carrier holes. Because of the wider energy gap of the barrier layer, extrinsic Shockley–Read–Hall (SRH) thermal generation–recombination (GR) dark currents are effectively suppressed. The idea of the nBn detector was proposed for III–V family compounds because of nearly zero valence band offset (VBO).[1–5]

Although HgCdTe is still regarded as the dominant semiconductor material for high-performance IR detectors, nBn photodetectors cannot be easily realized by use of these materials, because of the substantial VBO that characterizes HgCdTe-based heterostructures and the difficulties posed by heterostructure interface instability. These challenges are particularly difficult to overcome if HgCdTe-based nBn detectors are to be developed for operation in the long-wavelength infrared (LWIR) spectral range. Despite these problems, HgCdTe nBn devices operating in the mid-wavelength infrared (MWIR) range have been reported by Itsuno et al.,[6–8] who reported a planar nB_nn (*n*-type barrier) structure, grown by molecular beam epitaxy (MBE) on a bulk CdZnTe substrate, with a 5.7 μm cut-off wavelength.

The existence of the VBO limits the performance of HgCdTe-based nBn photodetectors because at low

(Received September 25, 2014; accepted November 1, 2014; published online December 2, 2014)

applied bias the valence-band discontinuity (ΔE_V) leads to an energy barrier in the valence band that inhibits flow of minority carrier holes from the absorber to the contact cap layer (Fig. 1a).[9] Depending on the wavelength of operation, a relatively high bias or "turn-on" voltage must be applied to the device to improve the efficiency of collection of photogenerated carriers. Consequently, further development of HgCdTe nBn photodetector technology will require substantial research on minimization or, preferably, elimination of the valence band barrier to realize the optimum nBn detector structure depicted in Fig. 1b. Ideally, the energy barrier ΔE_V encountered by minority carrier holes should be less than the average carrier thermal energy $(3/2k_BT)$, which is approximately 10 meV at 77 K.

In this paper, we present results from a numerical study of optimization of HgCdTe nBn structures for operation in the 3–5 μm MWIR and the 8–12 μm long-wavelength infrared (LWIR) spectral ranges. The work reported herein encompasses two nBn optimization strategies based on barriers formed by use of:

1. $Hg_{1-x}Cd_xTe$ alloys; and
2. $HgTe/Hg_{0.05}Cd_{0.95}Te$ type-III superlattices (T3SL).

METHOD OF CALCULATION

The spatial distribution of the band structure can be calculated from the electrostatic potential, Ψ, obtained by solution of the Poison equation under steady-state conditions. If the charge density ρ in the semiconductor structure does not depend on the gradient of the potential, Poisson's equation can be represented in the form:

$$\varepsilon_0 \nabla(\varepsilon \nabla \Psi) + e\rho = 0, \quad (1)$$

where $\rho = p - n + N_D^+ - N_A^-$, with p and n representing the hole and electron concentrations, respectively, and N_D^+ and N_A^- are, respectively, the concentrations of ionized donors and acceptors. Numerical solution of the nonlinear Poisson equation, Eq. 1, was achieved by using the diffusion-equation finite difference scheme described in Ref. 10. The energy values for the edges of the conduction and valence bands, E_C and E_V respectively, were calculated from the electrostatic potential, Ψ, the electron affinity, X, and the bandgap energy E_g, by use of the relationships:

$$E_C = -X - e\Psi, \quad (2)$$

and

$$E_V = -X - e\Psi - E_g, \quad (3)$$

This method was used to calculate the band diagram of the nBn device structures designed with barrier layers formed by use of HgCdTe alloys and

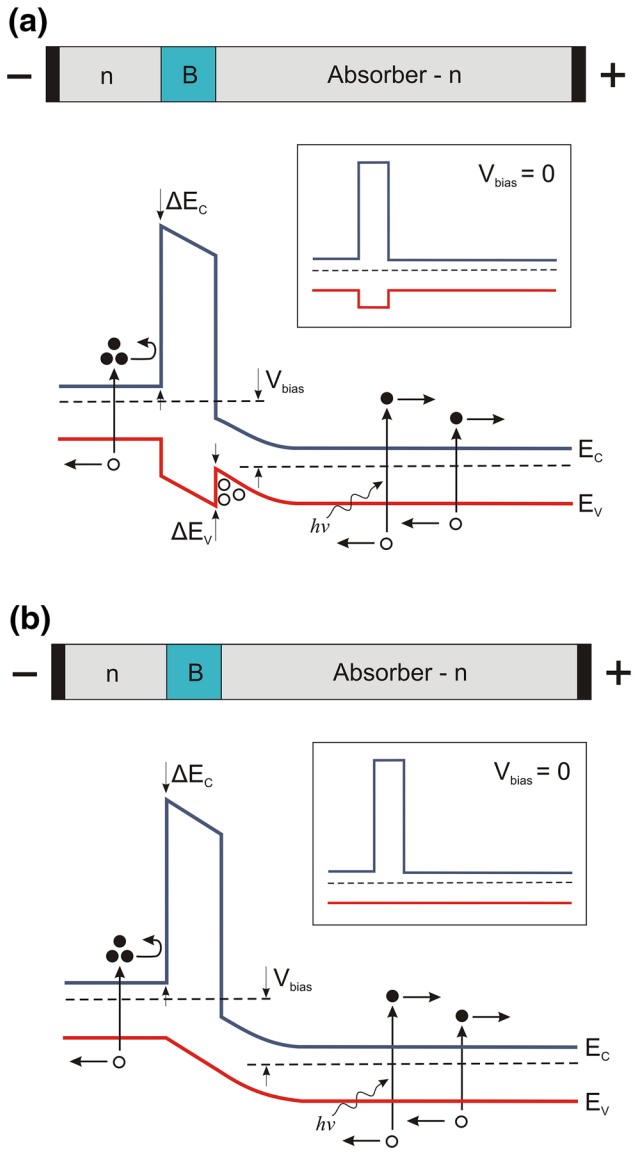

Fig. 1. Schematic band diagram for reverse-biased nBn detectors with (a) non-zero, and (b) zero VBOs. The conduction and valence band energy barriers are denoted ΔE_C and ΔE_V, respectively. Inset: band diagram under zero bias conditions.

by use of $HgTe/Hg_{0.05}Cd_{0.95}Te$ T3SL. For $HgTe/Hg_{0.05}Cd_{0.95}Te$ T3SL barriers, the calculations require the bandgap energy of the absorber, contact cap layers, the effective bandgap energy of the T3SL barrier region, and the corresponding valence band discontinuities as input data. The effective bandgap energy of the T3SL barrier region was assumed to coincide with the energy associated with the first heavy-hole to electron (HH1–C1) intersubband transition, calculated here by use of the envelope function approximation (EFA).[11,12] In this method, it is assumed that the relative positions of the energy band of the superlattice components, and hence, the VBO (Λ) between them, are known.

Self-Consistent Calculations for HgTe-$Hg_{0.05}Cd_{0.95}Te$ Band Alignment

The band positions of the HgTe/$Hg_{0.05}Cd_{0.95}Te$ T3SL constituent layers were calculated on the basis of self-consistent calculations, by use of Eqs. 1–3. Figure 2 shows the calculated alignments of the Γ_6 and Γ_8 bulk band edges for the HgTe-$Hg_{0.05}Cd_{0.95}Te$. These calculations assumed an n-type $Hg_{0.05}Cd_{0.95}Te$ layer doped at the level of $N_D = 1 \times 10^{15}$ cm^{-3} and a p-type HgTe layer doped at the level of $N_A = 1 \times 10^{15}$ cm^{-3}. Because of the high concentration of mercury vacancies, HgTe was assumed to be p-type. We obtained a HgTe-$Hg_{0.05}Cd_{0.95}Te$ VBO of approximately $\Lambda = 350$ meV at 80 K.

It is worth noting that the VBO between HgTe and CdTe has been the subject of a long-standing controversy. Magneto-optical measurements are indicative of a VBO of either 40 or 350 meV. Johnson and coworkers[13,14] demonstrated that either value could explain the magneto-optical results. The latter value (350 meV) was consistent with x-ray photoemission spectroscopy results, which average over the entire Brillouin zone.[15] Others determined much larger values of 530 meV and 450 meV at room temperature from k-resolved ultraviolet and x-ray photoemission at $k = 0$, and infrared absorption results, respectively.[16,17] Magneto-optical experiments[18] and photoluminescence spectra at liquid helium temperatures[19] suggested values of 800 meV and 650 meV, respectively. Λ was shown to be temperature dependent, i.e., $d\Lambda/dT = -0.40$ meV K^{-1}.[19] Consequently these values at liquid helium temperatures, in particular 650 meV, are in reasonably good agreement with room temperature values,[16,17] within published experimental uncertainties, e.g., ± 60 meV.

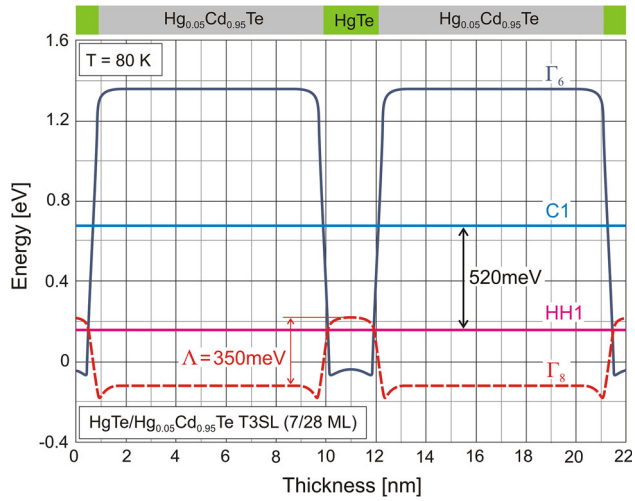

Fig. 2. Calculated band diagram for the 6-monolayer (ML) HgTe/28ML $Hg_{0.05}Cd_{0.95}Te$ superlattice and the HH1–C1 intersubband transition energy levels. The VBO obtained for HgTe-$Hg_{0.05}Cd_{0.95}Te$ is approximately 350 meV.

Calculation of the Energy Levels for the Barrier Made by T3SL

The superlattice electron and hole states are associated with the quantum well for electrons (solid line in Fig. 3) and the quantum well for holes (dashed line). The bottom of both quantum-wells is at the level of Γ_8 for the bulk HgTe. For these calculations, rectangular quantum-wells were assumed and different superlattice structures were considered with 28-monolayer (ML) of $Hg_{0.05}Cd_{0.95}Te$ and different thicknesses of HgTe layers. The thickness of the single ML for HgCdTe is approximately 0.324 nm. We consider only the growth direction of the superlattice in the center of the Brillouin zone. The $k{\cdot}p$ Hamiltonian can be regarded as decoupled in a such way that electrons, and heavy and light holes, can be considered independently.[11,20] Thus, the eigenvalues associated with these carriers can be obtained using a simple Kronig–Penney model.[21] Band properties for (211)B orientation are listed in Table I. HH1–C1 intersubband transition energy levels for the 2.27/9 nm HgTe/$Hg_{0.05}Cd_{0.95}Te$ T3SL, plotted on Γ_6 and Γ_8 bulk band edges, are shown in Fig. 2. The calculated HH1–C1 transition is approximately 520 meV.

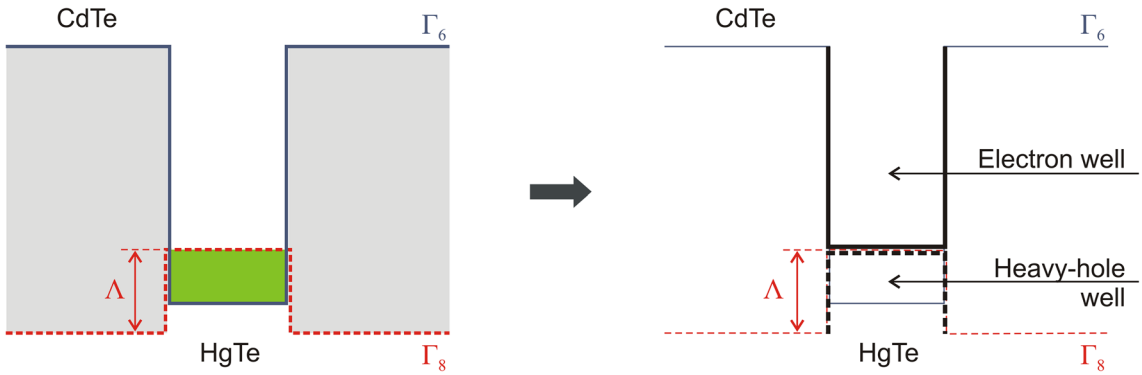

Fig. 3. Schematic diagram of energy band alignment in the HgT-CdTe system. Λ is the VBO. The superlattice electron and heavy-hole states are associated with the quantum well for electrons (solid line) and the quantum well for heavy holes (dashed line).

Table I. Band properties for (211)*B* orientation (m_0 is free electron mass)

Property	HgTe	$Hg_{0.05}Cd_{0.95}Te$
Electron effective mass (m_e^*)[20]	$0.031 \cdot m_0$	$0.11 \cdot m_0$
Heavy-hole effective mass (m_{hh}^*)[22]	$0.53 \cdot m_0$	$0.53 \cdot m_0$
Bandgap energy (E_g) at 80 K[23]	−0.260 eV	1.476 eV
Electron affinity (X) at 80 K[24]	4.508 eV	3.098 eV

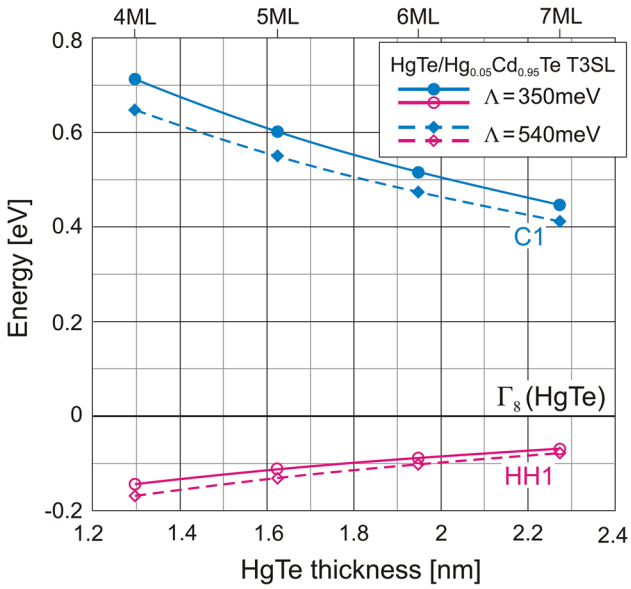

Fig. 4. Calculated HH1–C1 intersubband transition energy levels as a function of the thickness of the HgTe layer, calculated for two values of the VBO, Λ (350 meV and 540 meV). The thickness of the $Hg_{0.05}Cd_{0.95}Te$ layer remains the same, 9 nm. Zero energy is at the bottom of the quantum-well for electrons and heavy holes, at the level of Γ_8 for bulk HgTe (Fig. 3).

Figure 4 shows the HH1–C1 transitions as a function of the thickness of HgTe layer, keeping the thickness of the $Hg_{0.05}Cd_{0.95}Te$ layer constant at 28ML. Usually, the VBO is a fitting variable, but here we used the value of 350 meV, calculated in the initial estimations (Fig. 2, and described in the section "Self-consistent calculations for HgTe-$Hg_{0.05}Cd_{0.95}Te$ band alignment"). We also checked whether significantly modified HgTe/$Hg_{0.05}Cd_{0.95}Te$ VBO (here we chose 540 meV) can change the final trend line of the minibands positions. It is apparent that for both assumed values of the VBO, the energy of HH1–C1 transitions increase with reduction of the number of HgTe monolayers. What is more, the VBO does not significantly affect the position of the HH1 miniband, which is of crucial importance in determining the continuity of the valence band in nBn detectors.

BARRIER DESIGN

The numerical analysis was conducted by using a 3D model of a detector structure with an etched mesa topology. Figure 5 shows a 2D cross-section of HgCdTe nBn structure. The 1 μm thick cap contact layer and the 5 μm thick photon absorbing layers were defined as lightly doped ($N_D = 1 \times 10^{15}$ cm^{-3}) n-type HgCdTe with CdTe molar x-fractions $x_{Cap} = x_{Abs} = 0.235$ for the LWIR spectral range and $x_{Cap} = x_{Abs} = 0.315$ for the MWIR spectral range. For all the structures studied, the barrier layer was defined as 200 nm thick. Given that the barrier layer is sufficiently thick, tunneling has been neglected in this work.

Optimum design of the barrier layer composition and doping is crucial for nBn HgCdTe detector operation. The barrier layer must be thick enough and must also act as a sufficiently high energy barrier in the conduction band to minimize most of the carrier electron flow from the cap region to the absorber. It must also be a minimum energy barrier to minority carrier hole flow in the valence band to ensure collection of thermally and optically generated carriers moving from the absorber to the cap region.

Numerically calculated band diagrams for nBn structures formed with barriers made of HgCdTe alloys with CdTe mole fractions of $x_B = 0.6$, for MWIR detectors, and $x_B = 0.5$, for LWIR detectors, are shown in Fig. 6 for n- and p-type doping in the barrier region. From these calculations the valence band energy barrier at 80 K was found to be 100 meV for the MWIR device and 90 meV for the LWIR device, for undoped to relatively low n-doping densities. At low applied biases, this relatively high energy barrier ΔE_V effectively blocks diffusion of photogenerated holes from the absorber to the cap layer. In contrast, p-type doping of the barrier at the level of $N_A = 3 \times 10^{15}$ cm^{-3} results in a substantial decrease of the effective barrier ΔE_V to 60 meV for the MWIR structure and 50 meV for the LWIR structure. For both these, the conduction band barrier (ΔE_C) is sufficiently high to effectively block the flow of the electrons from the cap region to the absorber. As shown on current–voltage plots for the LWIR device (Fig. 7), the 330 meV conduction band barrier is sufficient to prevent electron flow under a wide range of applied reverse bias voltages. The barrier layer composition was $x_B = 0.6$ and $x_B = 0.5$ for the MWIR and for LWIR devices, respectively.

The composition, doping type, and concentrations in the barrier-layer have substantial effects on device performance. This is apparent from the calculated current–voltage characteristics presented in Figs. 7 and 8 for the LWIR nBn device structures. The dark

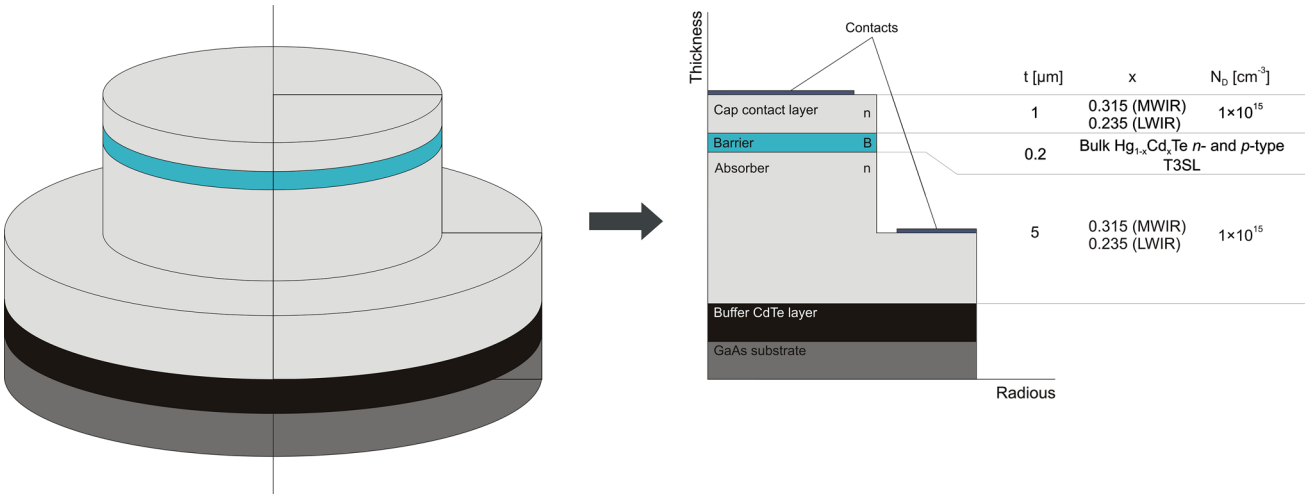

Fig. 5. Cross-section of the HgCdTe mesa structure.

current calculations include thermal generation mechanisms, Auger 1, Auger 7, and SRH through metal-site vacancies and dislocation related centers.[25] The metal-site vacancy concentration was assumed to be $N_T = 1 \times 10^{13}$ cm^{-3} with an ionization energy $0.75E_g$ above the valence band edge, and carrier capture cross-sections of $\sigma_n = \sigma_p = 5 \times 10^{-16}$ cm^2. The bulk dislocations density was assumed to be $G_{DIS} = 1 \times 10^5$ cm^{-2}, with the mean energy of the dislocation band at $0.32E_g$ above the valence band edge, and carrier cross sections equal to $\sigma_n = \sigma_p = 5 \times 10^{-15}$ cm^2. Figure 7 shows the effect of the composition of the n-type barrier-layer on the current–voltage characteristics of the LWIR nBn device. A composition whish is too low ($x_B = 0.35$) results in a significant increase in the current density, because only the 130 meV high conduction band barrier does not block the flow of the electrons sufficiently from the cap region to the absorber. An increase of the barrier composition to the $x_B = 0.5$ gives a conduction band barrier of 330 meV, resulting in saturation of the dark current. Further increase of the barrier composition does not change the value of saturation currents but increases the turn-on voltage. Therefore, the composition in the barrier layer should be chosen very precisely. In addition, the doping type and concentration levels in the barrier-layer also significantly affect the current–voltage characteristics of the nBn devices. As shown in Fig. 8, a high n-type doping concentration in the barrier layer reduces the rate of collection of holes and necessitates operation under higher applied reverse bias voltages. The turn-on bias is approximately 0.25 V for a detector with an $N_D = 5 \times 10^{15}$ cm^{-3} doped barrier layer. Lower donor concentrations in the barrier reduce the turn-on voltage to -0.1 V ($N_D = 1 \times 10^{15}$ cm^{-3}). In contrast, nBn devices with p-type doped barriers can operate at near zero-bias voltage.

Effective collection of minority holes is affected by both detector geometry and electric-field distribution. Calculated band diagrams and built-in electric field distribution for the zero-biased LWIR nBn structure for different doping conditions in the barrier are presented in Figs. 9 and 10. As expected, the maximum electric fields appear at the barrier-absorber and barrier-cap interfaces. Figure 11 illustrates the space-charge distribution in the nBn structure under different barrier-layer doping conditions under zero applied bias. It is noted that at the lower bandgap side of the absorber/barrier and barrier/cap layer regions an electron accumulation region is formed when the barrier is doped n-type, whereas a depleted space-charged region is formed when the barrier is doped p-type. For the n-type doped barrier, formation of the electron-accumulation layer also leads to an localized increase in the electric field that tends to further limit hole diffusion from the absorber to the cap layer, whereas for the p-type doped barrier, the space-charge region and its associated electric field aid in extraction and collection of holes generated within the absorber; this high electric-field region and depletion region results in enhanced rates of SRH thermal generation and, consequently, higher dark current (Fig. 8). Furthermore, the electric field can induce lowering of the effective activation energy of bulk and dislocation-related traps, thus degrading dark current through an increase in trap-assisted-tunneling (TAT) current components. Importantly, this implies that suppression of the extrinsic SRH thermal generation current components, which are deemed to be an attractive advantage of the nBn detector structure,[1] can only be exploited in structures with undoped or n-type doped barrier layers, which do not have depletion regions within the narrower gap absorber layer. As expected, because of the barrier-layer's wider bandgap, the calculated

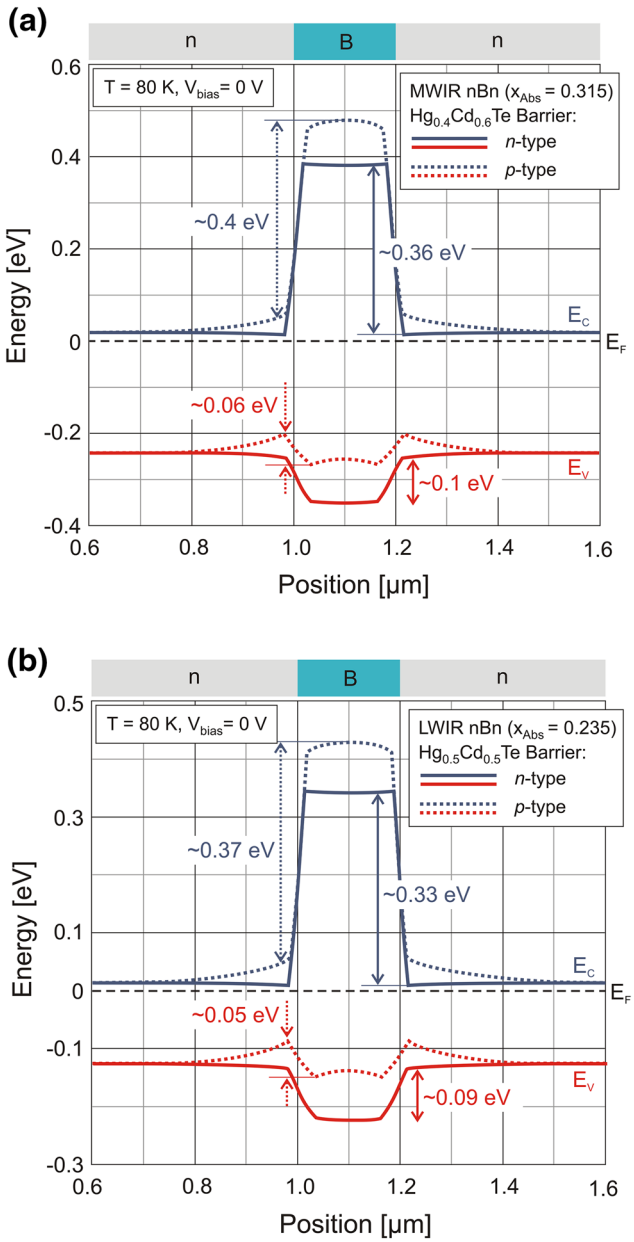

Fig. 6. Calculated equilibrium band diagrams for (a) MWIR and (b) LWIR HgCdTe nBn detectors with *n*-type ($N_D = 1 \times 10^{15}$ cm^{-3}) and *p*-type ($N_A = 3 \times 10^{15}$ cm^{-3}) doped barrier layers.

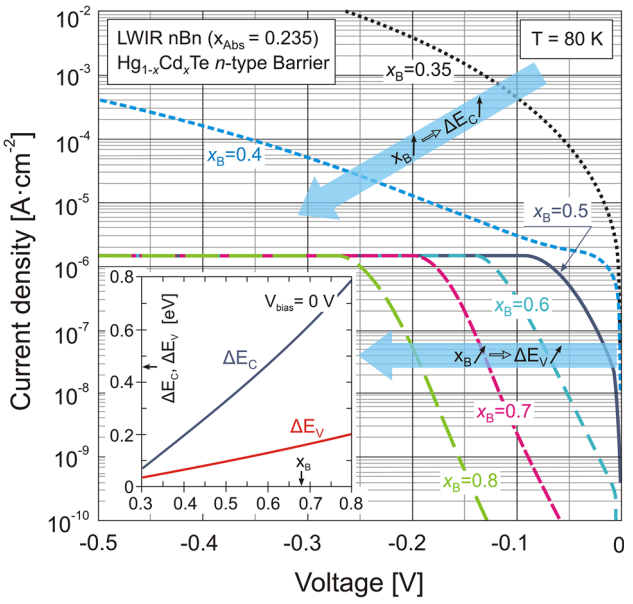

Fig. 7. Dark current–voltage characteristics of an HgCdTe nBn detector for different barrier layer composition at 80 K. The *n*-type barrier layer doping level is $N_D = 1 \times 10^{15}$ cm^{-3}. Inset: Conduction and valence band barrier heights (ΔE_C and ΔE_V) as a function of barrier layer composition at 80 K and zero bias.

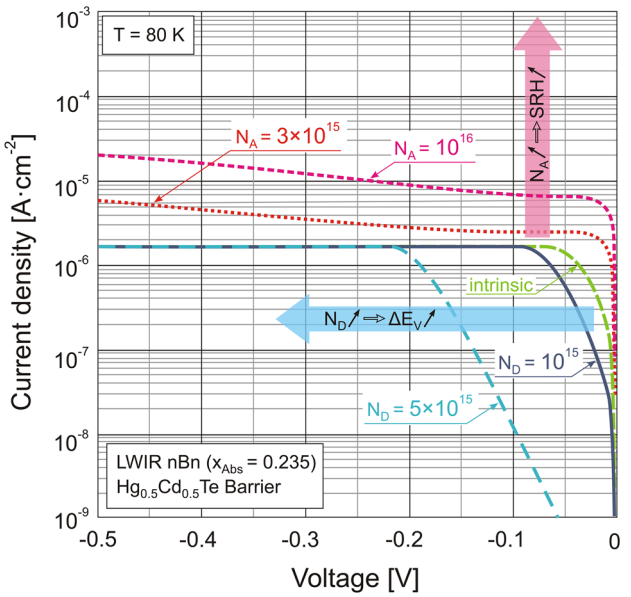

Fig. 8. Dark current–voltage characteristics of an HgCdTe nBn detector for different barrier layer doping conditions at 80 K. The composition of the barrier-layer is $x_B = 0.5$.

rate of SRH thermal generation in the barrier is negligible, as shown in Fig. 12.

Another significant disadvantage of *p*-type doped barriers is the technological challenge posed by dopant activation after MBE growth. For As, the most important acceptor impurity used in the growth of HgCdTe layers by MBE, the *ex situ* thermal annealing process required for As activation may have detrimental effects on the doping and composition profile of the structure.

An alternative approach to optimization of the barrier-layer energy profile, reducing the effective valence band energy barrier, to circumvent the need for *p*-type doping, is to use optimized HgTe/$Hg_{0.05}Cd_{0.95}Te$ superlattice barriers. Figure 13 illustrates the energy band diagrams calculated under zero bias conditions for MWIR and LWIR HgCdTe nBn detectors with barriers formed by use of two different superlattice designs. These results were obtained by assuming that the superlattice region can be approximated as a bulk-like layer with an effective HH1–C1 energy gap as indicated

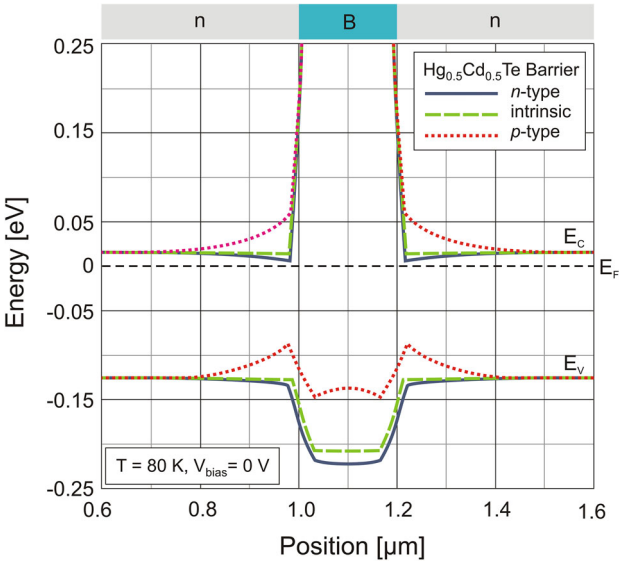

Fig. 9. Calculated band diagram for an LWIR HgCdTe nBn detector operated at 80 K under zero bias conditions.

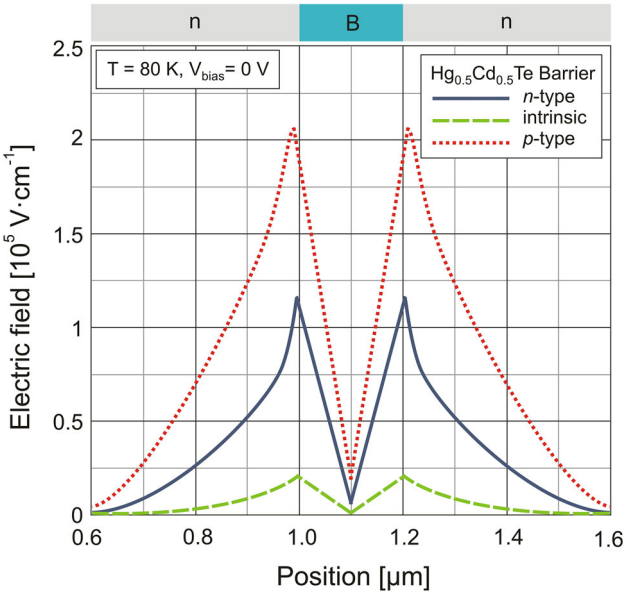

Fig. 10. Built-in electric field distribution in an LWIR HgCdTe nBn detector in the vicinity of the barrier layer region.

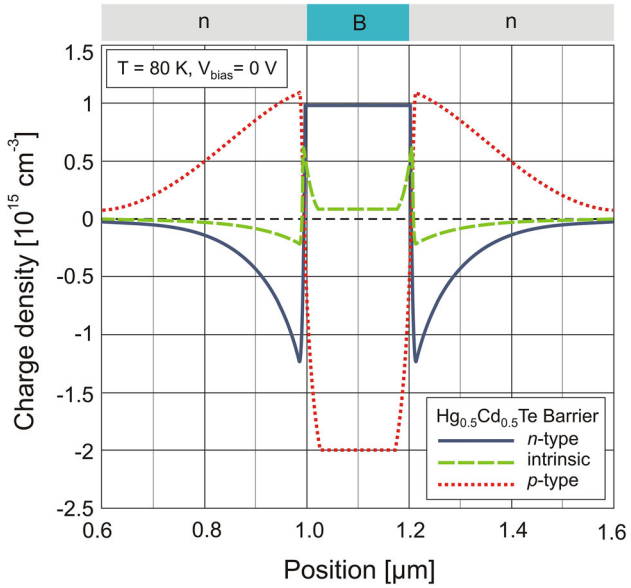

Fig. 11. Calculated space-charge regions in an LWIR HgCdTe nBn detector in the vicinity of the barrier layer.

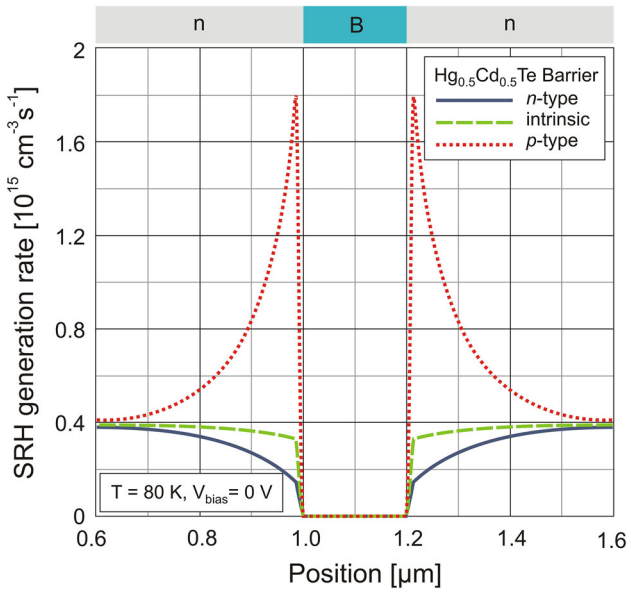

Fig. 12. Thermal generation in a LWIR HgCdTe nBn detector barrier layer in the vicinity of the barrier layer.

in Fig. 4 with $\Lambda = 350$ meV. According to these calculations the effective barrier-layer bandgaps are approximately 520 meV, for the 7ML of HgTe, 604 meV for 6ML, and 715 meV for 5ML. As is apparent from Fig. 13, the effective valence band energy barrier for the 6ML HgTe/28ML $Hg_{0.05}Cd_{0.95}Te$ barrier design for the MWIR detector and the 7ML HgTe/28ML $Hg_{0.05}Cd_{0.95}Te$ barrier design for the LWIR detector leads to a marginal potential well for holes that should not disrupt the efficiency of hole collection. This structure has an effective barrier in the conduction band of $\Delta E_c = 380$ meV for the MWIR detector and $\Delta E_c = 435$ meV for the LWIR detector. Reduction of the thickness of the HgTe layer by a single ML increases the effective barrier in the conduction band and simultaneously gives nearly zero offset in the valence band. On the basis of these calculations, nBn detectors with barriers formed by use of 5ML HgTe/28ML $Hg_{0.05}Cd_{0.95}Te$ and 6ML HgTe/28ML $Hg_{0.05}Cd_{0.95}Te$ superlattices are close to the optimum designs that meet the requirements for HgCdTe-based high-performance nBn detector technology for the MWIR and LWIR spectral ranges, respectively.

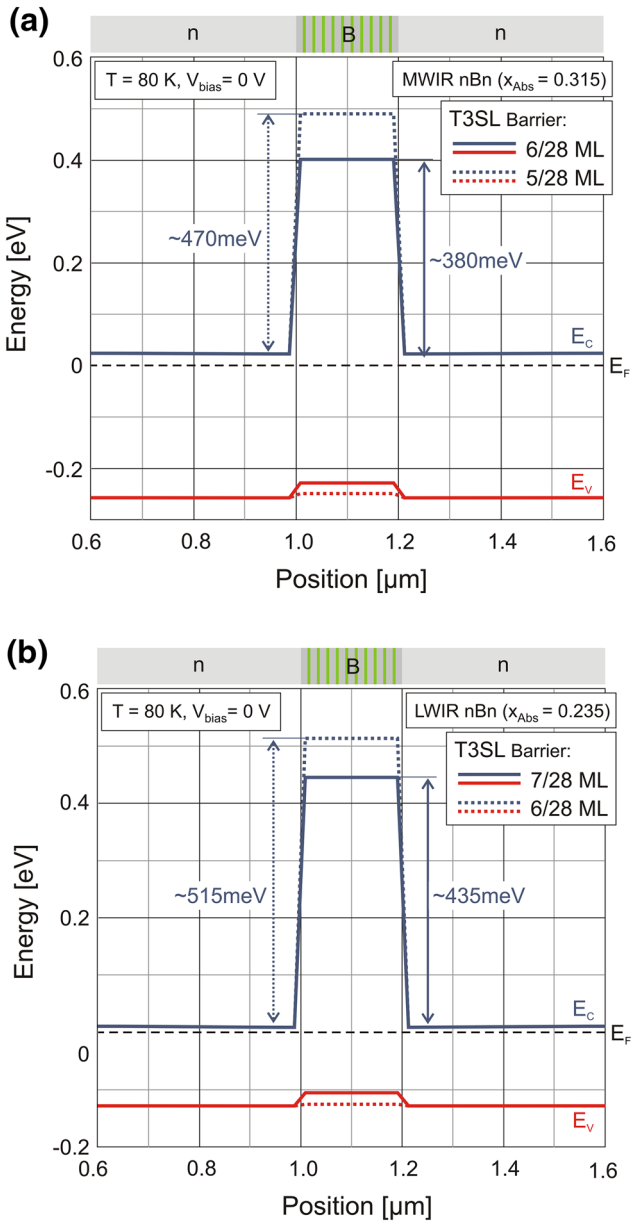

Fig. 13. Calculated zero bias energy band diagrams for (a) MWIR and (b) LWIR HgCdTe nBn detector with HgTe/$Hg_{0.05}Cd_{0.95}Te$ T3SL barrier layers. Calculations were performed for barriers with two distinct superlattice designs.

CONCLUSION

Lack of a zero VBO severely limits the theoretical performance of HgCdTe nBn detectors prepared by use of conventional abrupt HgCdTe-based barrier layers. Doping with donor impurities was found to increase the valence band energy barrier, leading to substantially lower minority carrier hole collection efficiency and require higher operating reverse bias. In contrast, *p*-type doping of the barrier layer induces a decrease in the effective valence band barrier encountered by minority carriers and results in detectors capable of operating at near zero-bias voltage. However, *p*-type doped barriers lead to formation of space–charge regions within the absorber region in the vicinity of the barrier/absorber interface, which results in higher dark currents because of SRH thermal generation, thus negating a crucial advantage of the nBn detector design. Our initial theoretical calculations presented in this paper indicate, however, that the HgTe/$Hg_{0.05}Cd_{0.95}Te$ superlattice may be an alternative means of realizing band-engineered barrier layers which overcome the problems posed by the relatively high valence band energy barriers formed by use of abrupt HgCdTe alloy designs.

ACKNOWLEDGEMENTS

The work was supported financially by Polish National Science Centre research Project No. DEC-2013/08/M/ST7/00913, Australian Research Council projects DP120104835 and FS110200022, and the WA-node of the Australian National Fabrication Facility.

OPEN ACCESS

REFERENCES

1. S. Maimon and G.W. Wicks, *Appl. Phys. Lett.* 89, 151109 (2006).
2. P. Klipstein, *Proc. SPIE.* 6940, 69402U-1 (2008).
3. D. Ting, A. Soibel, C. Hill, S. Keo, J. Mumolo, and S. Gunapala, *Proc. SPIE* 8353, 835332 (2012).
4. E. Plis, S. Myers, M.N. Kutty, J. Mailferd, E.P. Smith, S. Johnson, and S. Krishna, *Appl. Phys. Lett.* 97, 123503 (2010).
5. J.B. Rodriguez, E. Plis, G. Bishop, Y.D. Sharma, H. Kim, L.R. Dawson, and S. Krishna, *Appl. Phys. Lett.* 91, 043514-1 (2007).
6. A.M. Itsuno, J.D. Phillips, and S. Velicu, *Appl. Phys. Lett.* 100, 161102 (2012).
7. A.M. Itsuno, J.D. Phillips, and S. Velicu, *J. Electron. Mater.* 41, 2886 (2012).
8. S. Velicu, J. Zhao, M. Morley, A.M. Itsuno, and J.D. Philips, *Proc. SPIE* 8268, 82682X-1 (2012).
9. P. Maryniuk and A. Rogalski, *Solid-State Electron.* 80, 96104 (2013).
10. A. Jóźwikowska, *J. Appl. Phys.* 104, 063715 (2008).
11. G. Bastard, *Phys. Rev. B* 25, 7584 (1982).
12. F. Szmulowicz, E.R. Heller, K. Fisher, and F.L. Madarasz, *Superlattices Microstruct.* 17, 373 (1995).
13. P.M. Hui, H. Ehrenreich, and N.F. Johnson, *J Vac Sci Technol A* 7, 424 (1989).
14. N.F. Johnson, P.M. Hui, and H. Ehrenreich, *Phys. Rev. Lett.* 61, 1993 (1988).
15. R. Sporken, S. Sivananthan, J.P. Faurie, D.H. Ehlers, J. Fraxedas, L. Ley, J.J. Pireaux, and R. Caudano, *J. Vac. Sci. Technol. A* 7, 427 (1989).
16. D. Eich, K. Ortner, U. Groh, Z.H. Chen, C.R. Becker, G. Landwehr, R. Fink, and E. Umbach, *Phys. Stat. Sol. (a)* 173, 261 (1999).
17. C.R. Becker, V. Latussek, A. Pfeuffer-Jeschke, G. Landwehr, and L.W. Molenkamp, *Phys. Rev. B* 62, 10353 (2000).
18. K.H. Yoo, R.L. Aggarwal, L.R. Ram-Mohan, and O.K. Wu, *J. Vac. Sci. Technol. A* 8, 1194 (1990).
19. Z. Yang, Z. Yu, Y. Lansari, S. Hwang, J.W. Cook Jr, and J.F. Schetzina, *Phys. Rev. B* 49, 8096 (1994).

20. N.F. Johnson, H. Ehrenreich, P.M. Hui, and P.M. Young, *Phys. Rev. B* 41, 3655 (1990).
21. G. Bastard, *Wave mechanics applied to semiconductor heterostructures*, (Les Éditions de Physique, Les Ulis, 1988).
22. M.H. Weiler, *Semiconductors and Semimetals*, vol. 16, ed. R.K. Willardson and A.C. Beer, (Academic Press, New York, 1981), p. 119.
23. G.L. Hansen, J.L. Schmit, and T.N. Casselman, *J. Appl. Phys.* 53, 7099 (1982).
24. The Material Libraries in Commercial Program, Semicad Devices V.1.2, Down Technologies 1994.
25. K. Jóźwikowski, M. Kopytko, and A. Rogalski, *J. Appl. Phys.* 112, 033718 (2012).